http://www.press.ierek.com

ISSN (Print: 2357-0849, online: 2357-0857)

Environmental Science and Sustainable Development

Research Paper

Received:07 October 2025, Accepted: 21 December 2025, Published online: 31 December 2025

DOI: 10.21625/essd.v10i4.1249

Evaluation of Dye-Sensitized Solar Cells using Rutile-Mesoporous-SiO_2@TiO_2/CQDs as Scattering Layer

Kozo Taguchi[a*], Naoki Ikemoto[b], Trang Nakamoto[c]

[a] *Professor, Graduate School of Science and Engineering, Ritsumeikan University, Shiga, Japan*

[b] *Master, Graduate School of Science and Engineering, Ritsumeikan University, Shiga, Japan*

[c] *Assistant Professor, Graduate School of Science and Engineering, Ritsumeikan University, Shiga, Japan*

Abstract

Global warming is one of the most pressing environmental challenges worldwide. Dye-sensitized solar cells (DSSCs) have garnered significant attention as an eco-friendly alternative for energy generation, as they produce electricity without emitting greenhouse gases. Achieving a breakthrough in DSSC efficiency is crucial for overcoming the performance ceiling of conventional photoanodes. This work presents a highly scalable and simple light-harvesting strategy that significantly advances the state of the art in TiO_2-based composite architectures. In this study, we investigated the impact of incorporating Rutile-Mesoporous-SiO_2@TiO_2/carbon quantum dots (CQDs) particles into the scattering layer of DSSCs. The synthesized particles were characterized using scanning electron microscopy (SEM), energy-dispersive X-ray spectroscopy (EDS), X-ray diffraction (XRD), and UV–Vis spectroscopy. Their performance as a component of DSSCs was also evaluated in terms of power conversion efficiency. SEM analysis revealed that the addition of CQDs induced distinct surface irregularities, which were not observed in the undoped samples. UV–Vis measurements demonstrated that Rutile-MP-SiO_2@TiO_2/CQDs particles exhibited higher reflectance in the 380–780 nm range compared to their CQD-free counterparts. Furthermore, the proposed Rutile-MP-SiO_2@TiO_2/CQDs scattering layer markedly enhanced light scattering, yielding a 32.77% higher power density than cells with Anatase-MP-SiO_2@TiO_2. This simple and effective strategy overcomes conventional limitations and enables high-performance DSSCs.

© 2025 The Authors. Published by IEREK Press. This is an open-access article under the CC BY license (https://creativecommons.org/licenses/by/4.0/). Peer review under the responsibility of ESSD's International Scientific Committee of Reviewers.

Keywords

DSSC; SiO_2; TiO_2; CQDs;Light-scattering layer

1. Introduction

With the world's population growing and the demand for energy resources increasing, global warming and the depletion of fossil fuels have become pressing issues. The focus has shifted towards a promising energy solution: solar cells. These cells offer a sustainable approach as they harness renewable energy without emitting greenhouse gases. Notably, dye-sensitized solar cells (DSSCs) stand out as an affordable option in this category (Gong et al, 2012).

DSSCs are created using transparent electrodes, counter electrodes, dyes, electrolytes, and semiconductor materials (Prabavathy et al, 2017). The underlying mechanism involves the absorption of sunlight by a dye-infused semiconductor. This process triggers the release of electrons from the dye, which are then propelled into the conduction band and subsequently captured at the counter electrode. The electrolyte plays a crucial role in replenishing the dye through a regenerative process. Simultaneously, a reduction reaction takes place at the counter electrode, ensuring the electrolyte's continuous functionality (Karim et al, 2019; Hamann et al, 2011). TiO2 is a well-studied semiconductor material used in DSSC. This is because TiO2 has a large surface area and can adsorb most commonly used dyes (Hossain et al, 2018). To further enhance the efficiency of DSSCs, numerous studies have investigated methods to improve light harvesting and reduce charge recombination. Specifically, the incorporation of a dedicated scattering layer into the active layer has been shown to be an effective strategy for mitigating the recombination effect and enhancing performance by increasing the scattering capability (Mustafa & Sulaiman, 2021; Lee et al, 2009).

This research introduces a novel material, Rutile Mesoporous SiO_2@TiO_2 integrated with Carbon Quantum Dots (CQDs) as the light-scattering layer in DSSCs. Prior studies have established that controlling the photoanode structure and material phase is essential for optimizing DSSC performance. For example, incorporating a mesoporous SiO_2 framework into the photoanode has been shown to markedly increase the surface area for dye adsorption, thereby boosting current density and overall efficiency (Nakamoto et al, 2023a). Building on this surface-area enhancement strategy, another study (Nakamoto et al, 2023b),(Muhammad et al, 2018) examined the crystal phase and demonstrated that the Rutile phase offers higher light reflectivity than Anatase, resulting in a clear improvement in power output. However, this precursor work (Nakamoto et al, 2023b) optimized only the Rutile-Mesoporous-SiO_2@TiO_2 structure and did not incorporate the multi-functional benefits of CQDs. To address the need for a highly efficient, multi-functional light-scattering material, we propose a novel composite architecture that significantly advances the work of Nakamoto et al (2023b) by integrating CQDs to further enhance light harvesting.CQDs are one of the nanomaterials that have attracted much attention in recent years. Doping rutile-MP-SiO_2@TiO_2 with CQDs was considered to improve the absorption rate, which is a drawback of the rutile type. We thought that CQDs could be converted efficiently because of their stable optical absorption (Wang & Hu, 2014). This is also because the loss of doped CQDs when annealed at 990 °C is thought to roughen the surface of the particles, which is thought to increase diffuse reflection and improve reflectance properties.

2. Materials and Methods

2.1 Carbon Quantum Dots (CQDs)

First, it involved the meticulous mixing of 0.768 g of citric acid and 0.72 g of urea with 20 ml of purified water, followed by a thorough 20-minute stirring process. Next, the synthesized solution was then hydrothermally synthesized at 200 °C for 8 hours. Finally, the hydrothermally synthesized solution was filtered to obtain the CQDs solution. This solution was stored in a refrigerator.

2.2. Mesoporous SiO_2 (MP-SiO_2)

First, the addition of 3 ml of tetraethyl orthosilicate and 1.2 ml of octadecyltrimethoxysilane to 60 ml of ethanol, followed by a 10-minute stirring period to achieve a transparent solution. Subsequently, 9 ml of ammonia was gradually introduced at a rate of 0.5 ml/min while stirring, and the mixture was then stirred for an extended 1-day period. Finally, the collection of particles through centrifugation, followed by three ethanol washes. The particles were then subjected to a 60 °C drying process for a full day, ensuring their readiness for further analysis.

2.3. Anatase Mesoporous SiO_2@TiO_2 (A-MP-SiO_2@TiO_2)

First, 0.6 ml of titanium(IV)tetrabutoxide and 60 ml of ethanol were stirred for 10 min to obtain a clear solution. The subsequent steps were meticulously executed: 0.6g of the prepared MP-SiO_2 was introduced into the solution and subjected to ultrasonic dispersion for 15 minutes. Then, 1.2 ml of purified water was gradually added at a rate of 20

µl/min, followed by a 6-hour stirring period. The particles were then isolated through centrifugation, washed thrice with ethanol, and dried at 60 °C for half a day. Finally, it involved annealing the dried particles at 900 °C for 2 hours.

2.4. Rutile Mesoporous SiO_2@TiO_2/CQDs (Ru-MP-SiO_2@TiO_2/CQDs)

First, 1.5 ml of titanium (IV) tetrabutoxide and 60 ml of ethanol were stirred for 10 min to obtain a clear solution. The subsequent steps were meticulously executed: 0.6 g of the prepared MP-SiO_2 was introduced into the solution and subjected to ultrasonic dispersion for 15 minutes. Then, 3 ml of CQDs was gradually added at a rate of 20 µl/min, followed by a 6-hour stirring period. The particles were then isolated through centrifugation, washed thrice with ethanol, and dried at 60 °C for half a day. Finally, it involved annealing the dried particles at 990 °C for 4 hours.

2.5. Photoanode

Figure 1 illustrates the process of electrodeposition and spin-coating. FTO glass was used as the base for photoanodes. The active layer's preparation commenced with the utilization of commercially sourced TiO_2 (P25) nanoparticles. The electrodeposition solution underwent a 24-hour preparation process involving the stirring of 0.2g of P25 in 40 ml of ethanol, ensuring a homogeneous mixture. Electrodeposition was performed at 0.12mA for 100s using the prepared solution. The electrodeposition FTO glass was then annealed at 500 °C for 1 hour. This process yielded active layers of 10µm.

The spin-coating technique was employed to meticulously craft the scattering layer, positioned directly above the active layer. For the spin-coating method, 0.15g of Ru-MP-SiO_2@TiO_2/CQDs was mixed with 2.75 ml of isopropanol, 27.5µl of Triton-X, 55 µl of titanium tetraisopropoxide, 27.5mg of polyethylene glycol, and 2g of Zirconia balls were added to the mixture and stirred for 5 h 15 min to form a paste. Then, 0.6ml of the pasted solution was dropped onto the active layer and spin-coated for 1 minute. A scattering layer of 2µm to 3µm was obtained by this process. The scattering layer, once formed, underwent a heat treatment process at 500 °C for an hour, ensuring its stability and structural integrity.

A day-long immersion process was employed for the photoanodes, ensuring a comprehensive interaction with the dye solution. The preparation of the dye solution required a precise combination of 10mg of cis-bis(isothiocyanato)(2,2'bipyridyl-4,4'-dicarboxlato)(4,4'-dinonyl-2'-bipyridyl) ruthenium(II) dye and 0.442g of CDCA, mixed with 28.5 ml of acetonitrile and an equal volume of t-butyl alcohol, followed by a 10-minute stirring process.

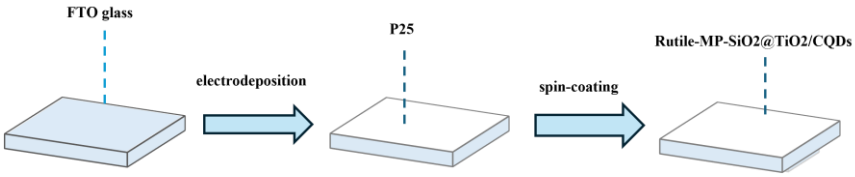

Figure. 1. Electrodeposition and spin-coating process. (Source: by authors)

2.6. Counter electrode and gel electrode

The counter electrode's foundation was constructed using an economical and adaptable stainless-steel mesh, offering both cost-effectiveness and versatility. The carbon ink application process involved immersing the stainless-steel mesh for 5 minutes, followed by a thorough drying period at 60 °C for 2 hours, ensuring optimal coverage. This study opted for gel electrolytes over aqueous alternatives to ensure long-term stability and reliability. For the electrolyte, 3 ml of electrolyte solution and 0.6 ml of propylene carbonate were stirred at 80 °C for 1 hour, and 0.5g of PMMA was added in triplicate during stirring. The drying phase was executed at 70 °C for a duration of 3.5 hours, ensuring the mixture's stability and readiness for the next steps. The electrolyte solution was obtained by stirring 0.507g of iodine with 0.133g of lithium iodide, 10 ml of acetonitrile, 1.59g of 1,2-Dimethyl-3-propylimidazolium Iodide, and 0.732 ml of 4-test-Butylpyridine for 30 minutes.

2.7. Creating DSSC

Figure 2 illustrates the steps involved in fabricating a DSSC. First, a photoanode with dye absorbed on it was taped to prevent short circuits except for the adsorbed film. The subsequent steps involved the precise placement of the gel electrolyte onto the adsorbed membrane, followed by the addition of a stainless steel mesh, immersed in carbon ink, which was then carefully secured with tape and a clip.

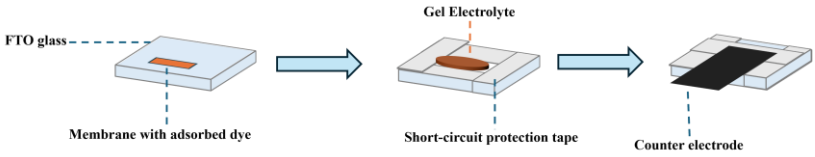

Figure. 2. Fabrication process of DSSC. (Source: by authors)

2.8. Evaluation Method

Ru-MP-SiO_2@TiO_2/CQDs particles were attached to the glass, then sputtered with gold and observed by SEM (S-4300, Hitachi, Ltd). EDS was employed to unravel the intricate composition of the particles, providing valuable insights into their elemental makeup. The reflectance of the particles was measured using a spectrophotometer. XRD was used to confirm the crystalline state of the particles. Reflectance spectra were measured using a spectrophotometer, based on n = 3 independent samples for Ru-MP-SiO_2@TiO_2/CQDs and Ru-MP-SiO_2@TiO_2, and n = 2 for A-MP-SiO_2@TiO_2. Results are presented as mean values with corresponding error bars.

DSSC voltage measurements, DSSCs were evaluated under illumination from a halogen lamp (MegaLight 100), adjusted to 3300 lx, and calibrated using a digital light meter (MT-921 LIGHT METER) before each measurement. All measurements were conducted in a controlled indoor environment (approximately 22 °C). The active cell area was fixed at 0.20 cm^2. Voltage–current characteristics were obtained by varying the external load from 300 kΩ to 800 Ω, and the power density was calculated based on the effective area. For the Ru-MP-SiO_2@TiO_2 sample, four DSSC cells were tested, whereas three cells were measured for the Ru-MP-SiO_2@TiO_2/CQDs and A-MP-SiO_2@TiO_2 samples. Because an indoor low-illuminance light source was used, the power density results are not directly comparable to AM1.5G conditions and are instead evaluated under indoor-light performance metrics.

3. Experimental Results

3.1. Observation of particles

Figure. 3 are SEM images of particles of (a) Ru-MP-SiO_2@TiO_2 and (b) Ru-MP-SiO_2@TiO_2/CQDs. The presence of CQDs could not be confirmed in this SEM image. The unique properties of CQDs, attributed to their minuscule size, are thought to be the primary factor in this phenomenon. The particles in the figure. 3 (a) and (b) indicate that the particle size is 200nm to 400nm for both. Figure 3(b) appeared to have a larger surface area and a rougher texture compared to Figure 3(a). The surface area expansion through CQDs doping, coupled with the surface irregularities induced by annealing defects, is the key contributor to this observed effect.

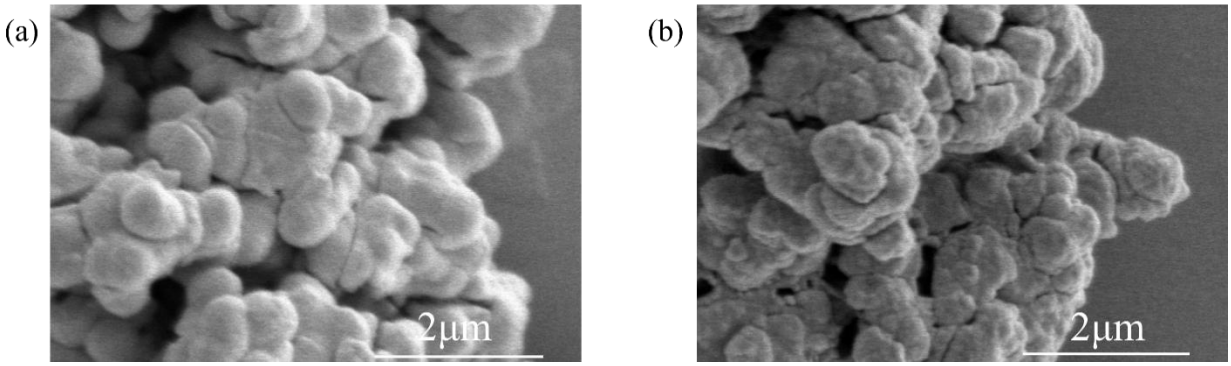

Figure. 3. SEM images of (a) Ru-MP-SiO_2@TiO_2 and (b) Ru-MP-SiO_2@TiO_2/CQDs. (Source: by authors)

3.2. Analysis of particle composition

Figure 4 provides a comprehensive visualization of the material's structure: (a) displays the SEM image of Ru-MP-SiO_2@TiO_2/CQDs, while (b), (c), and (d) offer mapping images of Si, Ti, and C, respectively, revealing intricate details of the composition. Figure 5 shows the EDS spectrum of Ru-MP-SiO_2@TiO_2/CQDs with peaks corresponding to C, O, Si, and Ti. The horizontal axis shows the X-ray energy, and the vertical axis shows the intensity. The results show that Ti exhibits the highest energy band, and C exhibits a small intensity in the lowest energy band. Table 1 shows the mass% of the chemical elements in the square in Figure 4 (a). The results show 7.82% of C, 18.76% of Si, and 25.77% of Ti. Although 7.82% of carbon was detected in the EDS analysis, this carbon is most likely derived from carbon residues produced during high-temperature treatment or from the carbon tape used for sample mounting. Given the high calcination temperature of 990 °C, it is unlikely that any functional CQDs remained after firing.

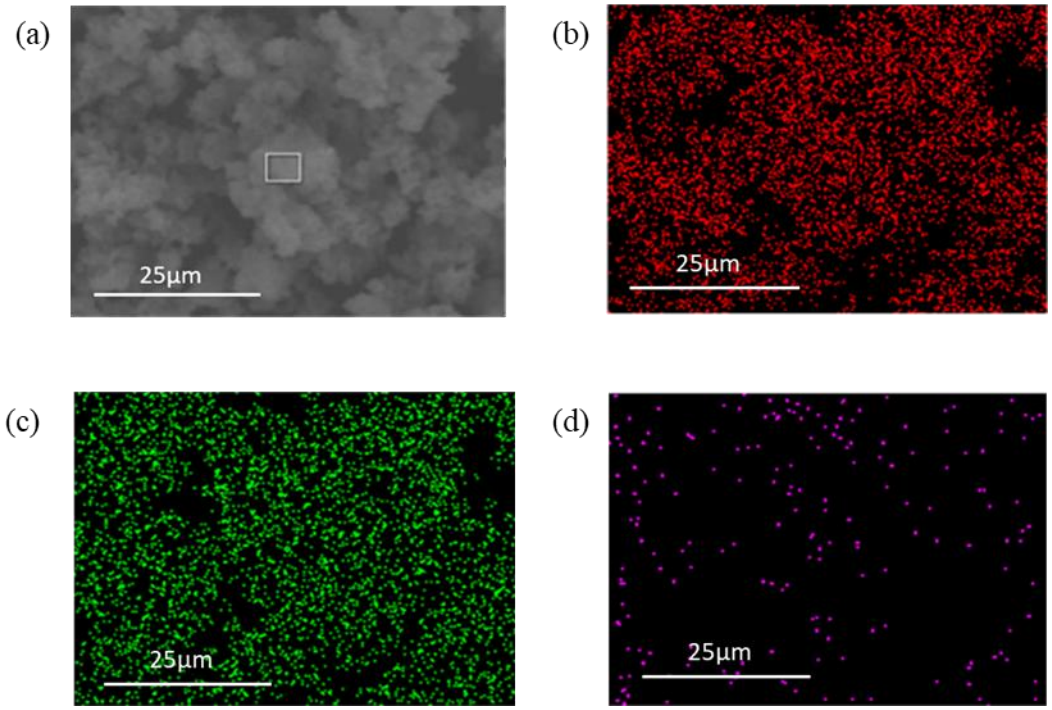

Figure. 4. (a) SEM image of Ru-MP-SiO_2@TiO_2/CQDs. EDS mapping images of (b) Si, (c) Ti, and (d) C. (Source: by authors)

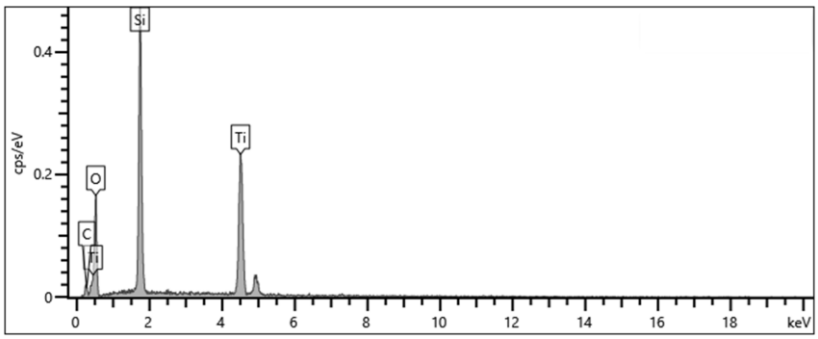

Figure. 5. EDS spectrum of Ru-MP-SiO_2@TiO_2/CQDs. (Source: by authors)

Table 1. Mass% of elemental compositions. (Source: by authors)

Chemical element	Mass (%)
C	7.82
O	47.65
Si	18.76
Ti	25.77
total	100.00

3.3. Evaluation of crystal structure by X-ray analysis

Figure 6 (a) illustrates the XRD pattern of the prepared Ru-MP-SiO_2@TiO_2/CQDs. From the XRD pattern, Ru-MP-SiO_2@TiO_2/CQDs exhibits high intensity even as the diffraction angle increases, confirming the presence of a peak representing the rutile phase. Figure 6 (b) shows the XRD pattern of the prepared Ru-MP-SiO_2@TiO_2. The XRD pattern shows a rutile phase peak as in Figure 6 (a), but the intensity is lower than that with CQD. Figure 6 (c) shows the XRD pattern of the prepared A-MP-SiO_2@TiO_2. The XRD pattern shows that there is a peak representing the anatase phase with a lower intensity as the diffraction angle increases.

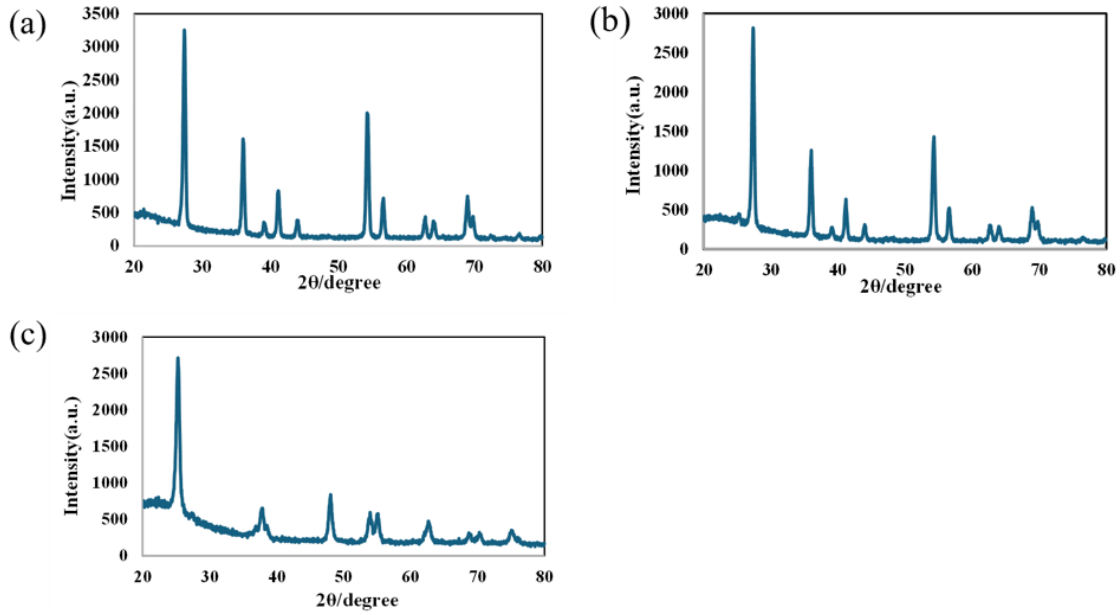

Figure. 6. XRD pattern of (a) Ru-MP-SiO_2@TiO_2/CQDs and (b) Ru-MP-SiO_2@TiO_2, (c) A-MP-SiO_2@TiO_2 (Source: by authors)

3.4. Evaluation of reflectance characteristics of Ru-MP-SiO_2@TiO_2/CQDs

Figure. 7 illustrates the reflectance characteristics of Ru-MP-SiO_2@TiO_2/CQDs, Ru-MP-SiO_2@TiO_2, and A-MP-SiO_2@TiO_2. In the visible light spectrum, Ru-MP-SiO_2@TiO_2 exhibited superior reflectance compared to A-MP-SiO_2@TiO_2. The data for A-MP-SiO_2@TiO_2 were based on n=2 measurements, with error bars representing the Min-Max range, while the data for Ru-MP-SiO_2@TiO_2 and the Ru-MP-SiO_2@TiO_2/CQDs composite were based on n=3 measurements, with error bars indicating the standard deviation ($\pm$ SD) of the replicates. The Ru-MP-SiO_2@TiO_2/CQDs composite demonstrated even more enhanced performance. The exceptional reflectance of Ru-MP-SiO_2@TiO_2/CQDs can be attributed to the higher refractive index of rutile relative to anatase, coupled with increased surface defects and diffuse reflections induced by CQD doping and subsequent high-temperature annealing.

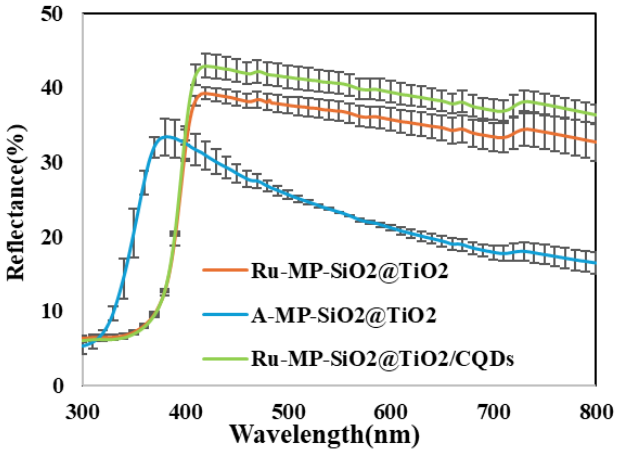

Figure 7. Reflectance spectra of the scattering layers: Ru-MP-SiO_2@TiO_2/CQDs, Ru-MP-SiO_2@TiO_2, and A-MP-SiO_2@TiO_2. (Source: by authors)

3.5. Evaluation of Ru-MP-SiO_2@TiO_2/CQDs on power density

Figure 8 illustrates the power density of DSSC with Ru-MP-SiO_2@TiO_2/CQDs and Ru-MP-SiO_2@TiO_2 and A-MP-SiO_2@TiO_2 as scattering layers. The performance data for Ru-MP-SiO_2@TiO_2/CQDs and A-MP-SiO_2@TiO_2 were obtained from n = 3 independent cells, while Ru-MP-SiO_2@TiO_2 was evaluated using n = 4 cells. All values are reported as the mean ± standard deviation (SD), and the error bars in Figure 8 represent the SD of the measurements. The maximum power density of Ru-MP-SiO_2@TiO_2 was 56.197 ± 0.522μW, indicating highly stable device performance. A-MP-SiO_2@TiO_2 exhibited a maximum power density of 48.644 ± 0.999μW, whereas incorporating CQDs into Ru-MP-SiO_2@TiO_2 led to a further improvement, achieving 64.581 ± 1.915μW.

In particular, Ru-MP-SiO_2@TiO_2/CQDs showed a 32.77% enhancement in maximum power density compared with A-MP-SiO_2@TiO_2. The observed trend is consistent with the reflectance measurements, suggesting that increased reflectivity contributes significantly to the improved DSSC performance.

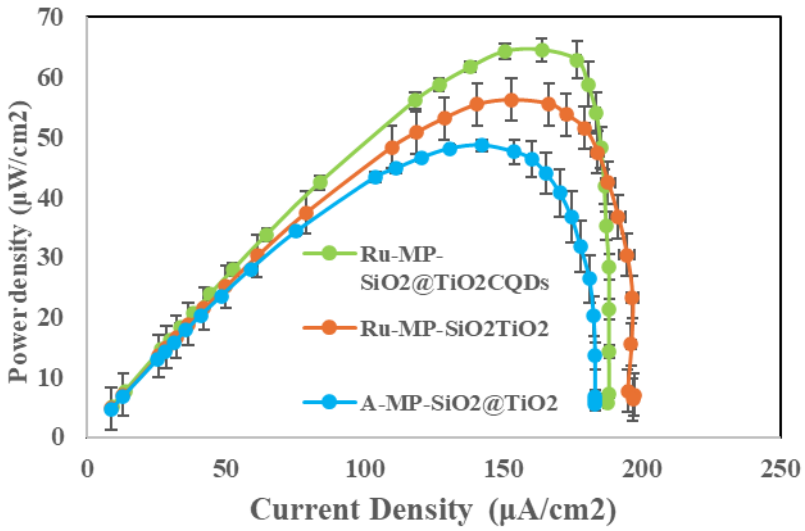

Figure 8. Power density of DSSC with Ru-MP-SiO_2@TiO_2/CQDs and Ru-MP-SiO_2@TiO_2 and A- MP-SiO_2@TiO_2 as scattering layers. (Source: by authors)

4. Conclusion

This research investigates the intricate relationship between particle composition, the reflectance properties of Ru-MP-SiO_2@TiO_2/CQDs, and the resulting power density of DSSCs, offering valuable insights into their interdependence. Ru-MP-SiO_2@TiO_2/CQDs were found to have excellent reflective properties in the scattering layer of DSSC. This indicates the effectiveness of Ru-MP-SiO_2@TiO_2/CQDs in the scattering layer of DSSC. The incorporation resulted in a 32.77% enhancement in maximum power density compared to the control sample (A-MP-SiO_2@TiO_2). The decomposition of the doped CQDs during the high-temperature annealing process is the primary cause for the enhanced scattering performance and resulting increase in DSSC power output, likely by inducing surface roughening of the particles. The power density measurements were intentionally conducted under a 3300 lx halogen lamp to mimic indoor low-light conditions relevant to IoT energy-harvesting applications. This provides practical insight into the real-world operating environment of the proposed device architecture. Future efforts will focus on structural optimization to further enhance light-harvesting efficiency. The next major objective is to construct a hollow Rutile@TiO_2 shell structure by etching out the internal SiO_2 core. Hollow structures are known to enhance light harvesting efficiency by promoting multiple reflections within the particles, thereby significantly lengthening the optical path. Concurrently, from a practical application perspective, it is necessary to evaluate the long-term stability and durability of the proposed structure, and to address challenges related to uniformity during scale-up to large-area cells.

Acknowledgements

The abstract of this paper was presented at the Green Urbanism (GU) Conference-9th Edition, which was held on the 25th – 27th of November 2025.

Funding declaration

This research did not receive any specific grant from funding agencies in the public, commercial, or not-for-profit sectors/individuals.

Ethics approval

Not applicable.

Conflict of interest

The authors declare that there is no conflict of interest regarding the publication of this paper.

References

Gong, J., Liang, J., & Sumathy, K. (2012). Review on dye-sensitized solar cells (DSSCs): Fundamental concepts and novel materials. Renewable and Sustainable Energy Reviews, 16(8), 5848-5860. https://doi.org/10.1016/j.rser.2012.04.044

Prabavathy, N., Shalini, S., Balasundaraprabhu, R., Velauthapillai, D., Prasanna, S., & Muthukumarasamy, N. (2017). Enhancement in the photostability of natural dyes for dye-sensitized solar cell (DSSC) applications: a review. International Journal of Energy Research, 41(10), 1372-1396. https://doi.org/10.1002/er.3703

Karim, N. A., Mehmood, U., Zahid, H. F., & Asif, T. (2019). Nanostructured photoanode and counter electrode materials for efficient Dye-Sensitized Solar Cells (DSSCs). Solar Energy, 185, 165-188. https://doi.org/10.1016/j.solener.2019.04.057

Hamann, T. W., & Ondersma, J. W. (2011). Dye-sensitized solar cell redox shuttles. Energy & Environmental Science, 4(2), 370-381.

Hossain, M. K., Pervez, M. F., Uddin, M. J., Tayyaba, S., Mia, M. N. H., Bashar, M. S., ... & Khan, M. A. (2018). Influence of natural dye adsorption on the structural, morphological, and optical properties of TiO2-based photoanode of dye-sensitized solar cell. Mater. Sci., 36, 93-101. https://doi.org/ 10.1515/msp-2017-0090

Mustafa, M. N., & Sulaiman, Y. (2021). Review on the effect of compact layers and light scattering layers on the enhancement of dye-sensitized solar cells. Solar Energy, 215, 26-43. https://doi.org/10.1016/j.solener.2020.12.030

Lee, J. K., Jeong, B. H., Jang, S. I., Kim, Y. G., Jang, Y. W., Lee, S. B., & Kim, M. R. (2009). Preparations of TiO2 pastes and their application to a light-scattering layer for dye-sensitized solar cells. Journal of Industrial and Engineering Chemistry, 15(5), 724-729. https://doi.org/10.1016/j.jiec.2009.09.053

Nakamoto, T., Higuchi, K., & Taguchi, K. (2023a). Effectiveness of Light Scattering Layer Using Mesoporous SiO2-TiO2 Core-Shell on Dye-Sensitized Solar Cells. IEEJ Transactions on Electrical and Electronic Engineering, 19(1), 157-159. https://doi.org/10.1002/tee.23938

Nakamoto, T., Higuchi, K., & Taguchi, K. (2023b). Investigation of Rutile and Anatase Mesoporous SiO2@ TiO2 Particles in the Scattering Layer of Dye-Sensitized Solar Cells. IEEJ Transactions on Electrical and Electronic Engineering, 19(2), 285-287. https://doi.org/10.1002/tee.23956

Muhammad, N., Zanoni, K. P. S., Iha, N. Y. M., & Ahmed, S. (2018). The Use of Rutile-and Anatase-Titania Layers towards Back Light Scattering in Dye-Sensitized Solar Cells. ChemistrySelect, 3(37), 10475-10482. https://doi.org/10.1002/slct.201801569

Wang, Y., & Hu, A. (2014). Carbon quantum dots: synthesis, properties and applications. Journal of Materials Chemistry C, 2(34), 6921-6939. https://doi.org/10.1039/C4TC00988F